Coupling of the FUN3D Unstructured Flow Solver and the LASTRAC Stability Code to Model Transition

Nathaniel Hildebrand*, Chau-Lyan Chang†, Meelan M. Choudhari‡, Fei Li§, and Eric Nielsen¶
NASA Langley Research Center, Hampton, VA, 23681

Balaji S. Venkatachari‖ and Pedro Paredes**
National Institute of Aerospace, Hampton, VA, 23666

We develop an iterative automated method to predict transition locations in boundary-layer flows by using the FUN3D solver to perform flow simulations and the LASTRAC code for linear stability computations. The coupling of FUN3D and LASTRAC allows for a robust physics-based approach to model boundary-layer transition by analyzing the growth of different instability waves and then using that information to iteratively update the resulting transition location. There is no user involvement during the iterative computations. We apply this automated method to subsonic flow over a flat plate with a sharp leading edge. The final solution has regions of laminar and turbulent flow with a transition onset location that agrees with experiments and stability-based correlations. This iterative automated method is also applied to an NLF(1)-0416 airfoil for conditions with and without a separation bubble. Along with predicting transition locations, we compare the streamwise distributions of surface-pressure and skin-friction coefficients to a transport-equation-based model. Finally, we show preliminary results of a 6:1 prolate spheroid at angles of attack equal to ten and fifteen degrees, where mixed-mode transition occurs due to Tollmien-Schlichting and crossflow instabilities.

Nomenclature

N	=	logarithmic amplification ratio
c	=	chord length (m)
L	=	streamwise length of the prolate spheroid (m)
M	=	Mach number
p	=	pressure (Pa)
Re_∞	=	freestream unit Reynolds number (1/m)
Re_c	=	Reynolds number based on the chord length
Re_L	=	Reynolds number based on the spheroid length
Pr	=	Prandtl number
T	=	temperature (K)
(u, v, w)	=	velocity components (m/s)
(x, y, z)	=	Cartesian coordinates (m)
β	=	spanwise wavenumber (1/m)
ρ	=	density (kg/m^3)
ω	=	angular frequency (rad/s)
C_f	=	skin friction
C_p	=	coefficient of pressure
C_D	=	drag coefficient

*Aerospace Technologist, nathaniel.j.hildebrand@nasa.gov, Computational AeroSciences Branch, AIAA Member
†Aerospace Technologist, chau-lyan.chang@nasa.gov, Computational AeroSciences Branch, AIAA Associate Fellow
‡Aerospace Technologist, meelan.m.choudhari@nasa.gov, Computational AeroSciences Branch, AIAA Fellow
§Aerospace Technologist, fei.li@nasa.gov, Computational AeroSciences Branch
¶Aerospace Technologist, eric.j.nielsen@nasa.gov, Computational AeroSciences Branch, AIAA Associate Fellow
‖Sr. Research Engineer, balaji.s.venkatachari@nasa.gov, Computational AeroSciences Branch, NASA LaRC, AIAA Senior Member
**Research Engineer, pedro.paredes@nasa.gov, Computational AeroSciences Branch, NASA LaRC, AIAA Senior Member

C_L = lift coefficient
Tu = turbulent intensity
K = kinetic-energy norm
α = angle of attack (°)
ϕ = azimuthal angle (°)

I. Introduction

The ability to accurately model transition to turbulence in boundary-layer flows is an important area of computational fluid dynamics (CFD) research that needs more attention in the future according to the NASA CFD Vision 2030 Study [1]. A few of the common approaches to study boundary-layer transition are direct numerical simulations (DNS), Reynolds-averaged Navier-Stokes (RANS) transition models, and wall-resolved large-eddy simulations (WRLES). The use of DNS or WRLES to study transition requires significant computational resources, especially if extended to high Reynolds numbers where the required grid resolution is extremely fine. Also, these simulations must have accurate initial and boundary conditions that come from either wind-tunnel measurements or flight tests. RANS models are much less computationally expensive than DNS and WRLES, but can be inaccurate for several reasons including their inability to capture the process of laminar-turbulent boundary-layer transition, which involves complicated physics including the receptivity, linear amplification, and the nonlinear interactions and breakdown of instability waves.

Semiempirical correlation-based methods that rely on linear stability theory (LST) are often used to predict transition locations in various flow configurations. The e^N method developed by Smith and Gamberoni [2] along with van Ingen [3] is commonly used and most cited in the literature. Transition occurs in the e^N method once the amplification factor reaches a critical value of N_{tr}. Here, the value of N_{tr} is determined by correlations with experiments. A well-known problem with the e^N method is that receptivity and nonlinear breakdown cannot be modeled accurately with just a single value of N_{tr}. Hence, variable N-factor methods have been proposed by Mack [4], and more recently by Crouch and Ng [5]. The parabolized stability equations (PSE) can also be used to predict transition to turbulence. These equations are less restrictive than linear stability theory because they do not require a parallel flow assumption [6]. LST and PSE can account for the amplification of Tollmien-Schlichting (TS) waves, stationary or traveling crossflow (CF) vortices, and other types of instability mechanisms.

There has been a lot of past work on coupling simulation tools with various stability methods [7–12]. These codes have been successful by taking advantage of RANS-based turbulence models, but they often do not resolve the boundary-layer profiles well in the laminar regions. It can also be difficult to couple unstructured CFD results with other numerical methods. The automated iterative approach in this paper uses a combination of basic states computed with FUN3D, an unstructured finite-volume RANS solver [13], and local stability analysis performed with LASTRAC, a state-of-the-art LST and PSE solver [14], to model boundary-layer transition. Note the basic states computed with FUN3D can have laminar, transitional, and fully-turbulent sections. The unstructured FUN3D data are given to LASTRAC via boundary-layer profiles, a surface grid, and inviscid streamlines. We determine the location of transition to turbulence in the FUN3D basic states with the LASTRAC stability calculations that involve computing N-factor envelopes across a broad range of frequencies and wavelengths with PSE. We enforce the new transition locations in the next FUN3D basic state that is followed once again by stability analysis, resulting in an iterative procedure. Our iterative approach is robust because we are taking into account the growth of different instability waves. It also does not take long to converge the transition location (both in terms of computational time and the number of iterations). We apply our iterative approach to a two-dimensional flat plate with a sharp leading edge and the NLF(1)-0416 airfoil with and without a separation bubble. Also, we present a preliminary analysis for the 3D 6:1 prolate spheroid at two different angles of attack, where CF effects become important (along with TS waves).

This conference paper is structured in the following manner. Section II explains the numerical methodology of our iterative approach, including the basic-state computations and the linear stability analysis. The flow configuration and results of the flat plate are presented in Section III, whereas the flow configuration and results of the NLF(1)-0416 airfoil are presented in Section IV. Preliminary results for the 6:1 prolate spheroid that includes CF instabilities are shown in Section V. We conclude this conference paper in Section VI.

II. Numerical Methodology

We use simulation tools and stability analysis with FUN3D [13] and LASTRAC [14], respectively, to model transition to turbulence in various flow configurations. This approach is more computationally expensive than using a

RANS-based transition model (e.g., Langtry-Menter four-equation shear-stress transport model [15]), but provides a complementary alternative and, for simple to moderately complex geometries, it may be more accurate by virtue of incorporating more of the physics associated with instability modes. It is also less computationally expensive than DNS and WRLES. We describe the components of the automated iterative method in the following subsections.

A. FUN3D Basic States

To compute the basic states, we utilize the suite of codes known as FUN3D, which is a node-centered unstructured-grid upwind-biased RANS solver [13]. This suite of codes has the ability to compute a laminar, transitional, or fully-turbulent basic state. In FUN3D, the inviscid terms are computed with a flux-difference-splitting scheme, and the viscous terms are evaluated with a finite-volume formulation. Pseudotime integration is performed with an implicit second-order Euler scheme. For the turbulent portions of the flow field, we use the Spalart-Allmaras (SA) one-equation model [16]. FUN3D allows a user to specify the exact location of transition along a boundary. The laminar region has the turbulent production terms switched off. For an example of how this works, see Lee-Rausch et al. [17] who studied transonic cruise of a DLR-F6. We run the FUN3D simulations until the residual has dropped to around machine zero. An example of this residual drop is depicted in Figure 1, which corresponds to a transitional flat-plate simulation with $U_\infty = 34$ m/s and $\mathrm{Re}_\infty = 2.26 \times 10^6$ m^{-1}. The location of transition onset for the flat-plate case in Figure 1 is $x_{\mathrm{tr}} = 1.168$ m. Figure 1 shows the residual drops approximately eleven orders of magnitude for both the density and streamwise velocity. Similar residual plots are obtained for the other flat-plate and airfoil simulations, but are not shown for brevity. The most recent version of the FUN3D manual [18] has detailed information about the different boundary conditions, numerical methods, and residual calculations used in this conference paper.

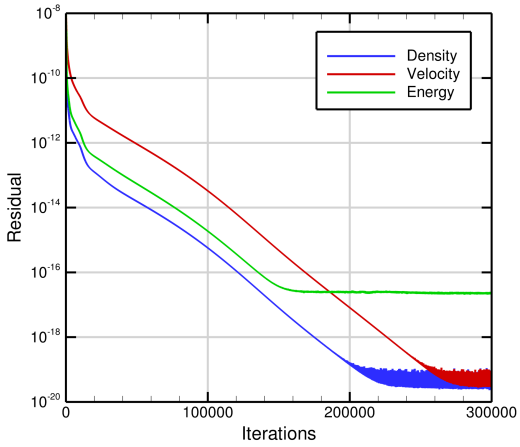

Fig. 1 Density, streamwise-velocity, and energy residuals versus the iteration number from a transitional flat-plate simulation at $U_\infty = 34$ m/s, $\mathrm{Re}_\infty = 2.26 \times 10^6$ m^{-1}, and $x_{\mathrm{tr}} = 1.168$ m with FUN3D.

B. LASTRAC Stability Calculations

We compute the linear disturbance amplification using PSE about the FUN3D basic states with LASTRAC [19]. The linear perturbations (assumed to be harmonic in both time and the spanwise direction) are defined as follows

$$\tilde{\mathbf{q}}(x, y, z, t) = \breve{\mathbf{q}}(x, y) \exp\left[\mathrm{i}\left(\beta z - \omega t\right)\right] + \mathrm{c.c.}, \tag{1}$$

where c.c. denotes the complex conjugate. Here, ω is the angular frequency, and β is the spanwise wavenumber. Also, $\tilde{\mathbf{q}}(x, y, z, t) = (\tilde{\rho}, \tilde{u}, \tilde{v}, \tilde{w}, \tilde{T})^{\mathrm{T}}$ and $\breve{\mathbf{q}}(x, y) = (\breve{\rho}, \breve{u}, \breve{v}, \breve{w}, \breve{T})^{\mathrm{T}}$. Pressure, density, and temperature are denoted by p, ρ, and T, respectively. The variables (x, y, z) denote the Cartesian coordinates. We denote (u, v, w) as the velocity components in the streamwise, wall-normal, and spanwise directions, respectively. PSE is used in our iterative approach because it accounts for streamwise variation of the boundary-layer thickness and shape of the disturbance field. Note that PSE numerically solves an approximate form of the Navier-Stokes equations for a slow-varying shape function and a complex streamwise wavenumber $\alpha(x)$ using the following relation

$$\breve{\mathbf{q}}(x,y) = \hat{\mathbf{q}}(x,y)\exp\left[\mathrm{i}\int_{x_0}^{x}\alpha(x')\,\mathrm{d}x'\right], \tag{2}$$

where the amplitude functions $\hat{\mathbf{q}}(x,y)$ vary slowly in the streamwise direction. We employ the boundary conditions $\tilde{u} = \tilde{v} = \tilde{w} = \tilde{T} = 0$ at the wall and $\tilde{u} = \tilde{w} = \tilde{T} = \tilde{\rho} = 0$ in the freestream for PSE.

According to linear stability theory, transition onset occurs at the streamwise location where the N-factor of any fixed-frequency or fixed-wavelength disturbance first reaches a critical value of N_{tr}. The N-factor is defined as

$$N(x) = \frac{1}{2}\ln\left[\frac{K(x)}{K(x_{\mathrm{lb}})}\right], \tag{3}$$

where x_{lb} denotes the lower-branch location where the disturbance at any given frequency and wavelength combination first becomes unstable and the kinetic-energy norm K is defined as

$$K(x) = \int_y (\breve{u},\breve{v},\breve{w})^{\mathrm{H}}\mathrm{diag}[\bar{\rho}(x,y),\bar{\rho}(x,y),\bar{\rho}(x,y)](\breve{u},\breve{v},\breve{w})\mathrm{d}y. \tag{4}$$

The superscript H denotes the Hermitian operator. We compute an envelope by finding the maximum N-factor at each streamwise station. Hence, the transition location is where N_{tr} intersects with the N-factor envelope. To find N_{tr} we compare to experimental measurements [20] or, if we know the turbulent intensity Tu, we can use the equation $N_{\mathrm{tr}} = -8.43 - 2.4\ln(Tu)$ from Mack [4]. We also use values of N_{tr} from the AIAA Transition Modeling Workshop 1 (`https://transitionmodeling.larc.nasa.gov/workshop_i/`).

C. Iterative Approach

A schematic of the automated iterative method used in this study is depicted in Figure 2. This method starts with computing an initial basic state with the FUN3D suite of codes. This could be a laminar basic state or a transitional basic state. If the basic state is transitional, we enforce the location(s) of transition onset far downstream. The converged FUN3D solution along with the computational grid is then converted via Python scripts to a solver-independent format that is given to LASTRAC, which involves the extraction of boundary-layer profiles and generation of numerous streamlines [21]. For more information about the solver-independent module, see the yellow box in Figure 2. Afterward, we employ the LASTRAC stability code to find the new location(s) of transition onset.

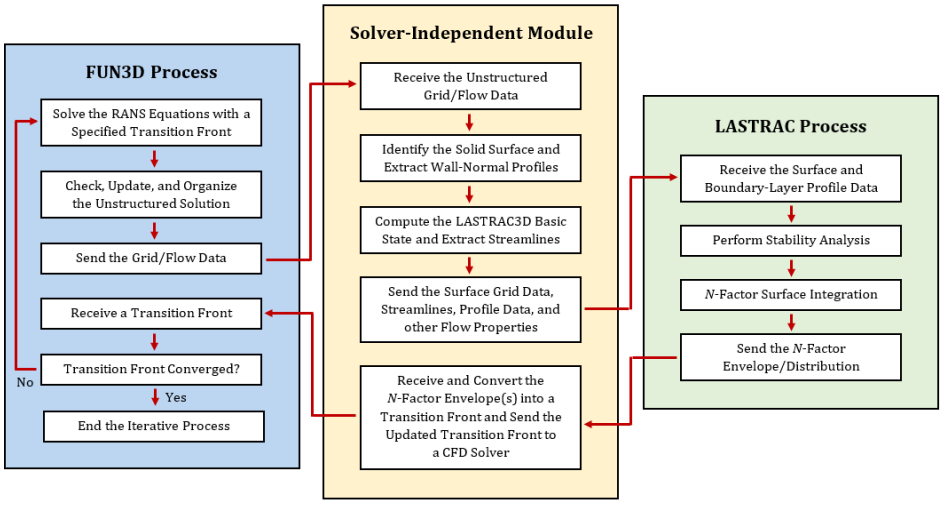

Fig. 2 Schematic of our iterative automated method with the FUN3D and LASTRAC codes.

For simple two-dimensional flow configurations, we compute the N-factor envelope(s) using LST or PSE with LASTRAC about the initial FUN3D basic state. We then find the streamwise location x_{tr} where N first reaches the

value of N_{tr} that is expected to correlate with the onset of transition in the flow configuration of interest. For more complicated three-dimensional flow configurations, we use LASTRAC to perform instability calculations about the initial FUN3D basic state and output the 2D or 3D N-factor distribution over the surface of interest. The predicted location(s) of transition onset is (are) then enforced in the next FUN3D basic-state computation, where the laminar region has the turbulent production terms switched off. Next, we compute the N-factor envelope/distribution about the new FUN3D basic state. This procedure is repeated until the location(s) of transition onset is (are) converged. For the current implementation in this paper, transition from laminar to turbulent flow happens abruptly, but in the future we have to use a smooth intermittency function.

For TS wave computations along each streamline, the wave angle is assumed to be zero at all locations. In other words, TS waves are assumed to follow the inviscid streamline for any given disturbance frequencies. PSE N-factor integration is carried out for each frequency without any optimization. The resulting N-factor envelope formed by various disturbance frequencies versus the arc length along each streamline is used to uniquely determine the N value at each streamline point. For stationary crossflow disturbances, a nonorthogonal coordinate is used at each point along the streamline, with the x-coordinate along the streamline direction and the spanwise ($z-$) direction chosen to be along the azimuthal grid line direction. For axisymmetric bodies such as the 6:1 prolate spheroid, an integer azimuthal wavenumber is imposed. Linear PSE computations are carried out for a range of integer wavenumbers to form an envelope. The resulting stationary crossflow or TS waves N-factor distribution along each streamline is imposed on the 3D surface. Planar interpolation (based on minimal distance to a discrete streamline point) of N-factors over the entire surface is used to determine the 3D surface transition location based on a predetermined transition N-factor criterion (e.g., dual N_{TS}-N_{CF} criterion [29, 30]).

III. Flat Plate

We consider subsonic flow over a two-dimensional flat plate with a sharp leading edge. The flat plate starts at $x = 0$ m and extends to $x = 2$ m. We select the flow parameters to match those of the Wang and Gaster [20] experiment. The freestream density, velocity, and temperature are $\rho_\infty = 1.206$ kg/m^3, $U_\infty = 34$ m/s, and $T_\infty = 292.7$ K, respectively. We assume a perfect gas so $p = \rho RT$, where $R = 287.15$ J/K/kg is the specific gas constant for air. Here, $\gamma = 1.4$ is the constant ratio of specific heats. The Prandtl number is set to a constant value of Pr = 0.72. To compute the dynamic viscosity μ, we use Sutherland's law with the Sutherland reference temperature $T_S = 110.4$ K. Figure 3 shows the laminar flat-plate basic state at the selected flow parameters. The left edge of the computation domain at $x = -0.15$ m is a subsonic inflow, and the right edge is a back-pressure outflow. Furthermore, the flat plate has adiabatic and no-slip boundary conditions, and the small portion before the flat plate is set to a wall-normal-symmetry boundary condition. We employ a freestream boundary condition at the top edge of the domain. A grid with 4000 points in the streamwise direction and 400 points in the wall-normal direction is used to resolve subsonic flow over a flat plate. The wall-normal direction extends to $y = 0.11$ m. We place the first grid point above the flat plate at a distance that satisfies $y^+ <= 0.1$ regardless of the boundary-layer state, and the wall-normal grid spacing increases gradually from there to the freestream. We also use grid stretching in the streamwise direction to resolve the start of the flat plate at $x = 0$ m. We compared skin-friction and pressure-coefficient distributions with resolutions of 500×50, 1000×100, 2000×200, and 4000×400 to confirm the results are grid converged (not shown).

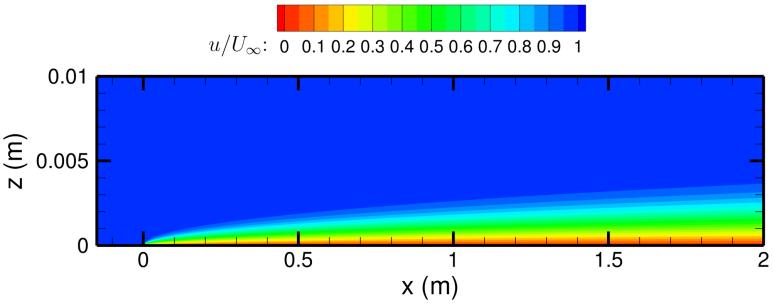

Fig. 3 Laminar flow over a flat plate computed with FUN3D at $U_\infty = 34$ m/s and $\text{Re}_\infty = 2.26 \times 10^6$ m^{-1}.

After solving for the initial laminar FUN3D basic state, we calculate the N-factor envelope with LASTRAC and find the corresponding location of transition onset. The left plot in Figure 4 shows the N-factor envelope computed with PSE

about the basic state in Figure 3. Notice the maximum N-factor is approximately equal to 11 at $x = 2$ m. This envelope has good agreement with the N-factor envelope corresponding to a flat-plate case at the same flow conditions in Figure 4 from Hildebrand et al. [22]. We know from our earlier study [22] that $N_{\text{tr}} = 7.6$ in order to obtain a transition location that matches experiments by Wang and Gaster [20]. Using this value of $N_{\text{tr}} = 7.6$, the initial FUN3D solution yields a location of transition onset at $x_{\text{tr}} = 1.133$ m. Accordingly, we enforce transition onset at $x_{\text{tr}} = 1.133$ m in the next FUN3D simulation. We compute the N-factor envelope about the new transitional FUN3D basic state using PSE with LASTRAC. From this new N-factor envelope, we get a transition location of $x_{\text{tr}} = 1.165$ m, which is enforced in the next FUN3D simulation. This process is repeated two more times yielding a final transition location of $x_{\text{tr}} = 1.168$ m. The right plot in Figure 4 displays four N-factor envelopes, each one computed about a different transitional FUN3D basic state. We can see the N-factor envelopes in Figure 4 eventually converge along with x_{tr}. Table 1 shows how the location of transition onset, the lift coefficient, and the drag coefficient all converge with iteration number for this flat-plate case.

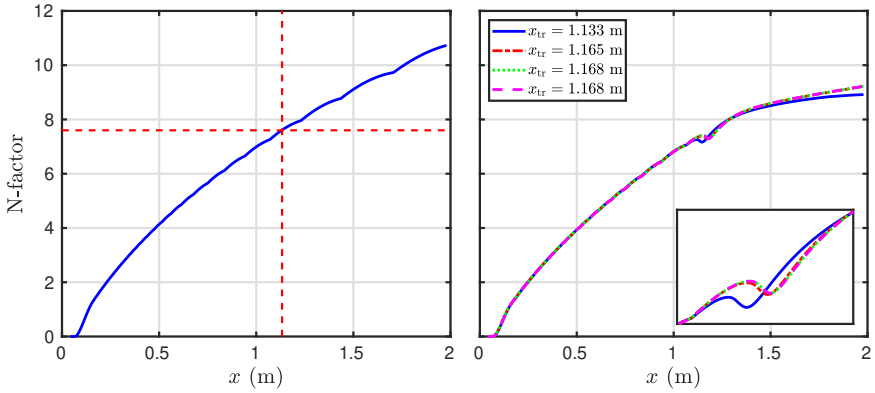

Fig. 4 N-factor envelopes computed with LASTRAC about several FUN3D basic states of flow over a flat plate at $U_\infty = 34$ m/s and $\text{Re}_\infty = 2.26 \times 10^6$ m^{-1}. The red dashed lines in the left plot indicate $N_{\text{tr}} = 7.6$ and the corresponding transition location of $x_{\text{tr}} = 1.133$ m for the laminar basic state. In the right plot, iteration one is the blue solid line, iteration two is the red dashed-dotted line, iteration three is the green dotted line, and the final iteration is the magenta dashed line.

Table 1 Convergence of the streamwise location of transition onset, the lift coefficient, and the drag coefficient with the iteration number for the flat-plate case using our automated iterative method in Figure 2.

Iteration #	x_{tr} (m)	C_L	C_D
0	N/A	-1.185×10^{-3}	1.250×10^{-4}
1	1.133	-2.608×10^{-3}	3.636×10^{-4}
2	1.165	-2.526×10^{-3}	3.549×10^{-4}
3	1.168	-2.515×10^{-3}	3.538×10^{-4}
4	1.168	-2.515×10^{-3}	3.538×10^{-4}

Figure 5 depicts the final transitional FUN3D basic state resulting from the automated iterative method. The boundary layer transitions at $x_{tr} = 1.168$ m in Figure 5. Note the intermediate transitional FUN3D basic states look identical to Figure 5, except the location of transition onset is slightly different. To better observe the location of transition onset and how it evolves with the iteration number, we plot the skin-friction distributions from laminar, transitional, and fully-turbulent basic states computed with FUN3D in Figure 6. The fully-turbulent case is run with the SA model [16]. For the first transitional basic state, notice how the skin friction starts at the laminar value and then increases rapidly to a turbulent value at $x_{\text{tr}} = 1.133$ m. There is a small overshoot in the skin friction at the location of transition onset for the transitional basic states. We see in Figure 6 that after the third iteration of the procedure outlined in Figure 2, the location of transition onset is converged. A close-up view of the skin-friction plots near $x = 1.168$ m in

Figure 6 shows the minor differences between the second, third, and fourth iteration. These results for subsonic flow over a two-dimensional flat plate demonstrate the effectiveness of an iterative automated method.

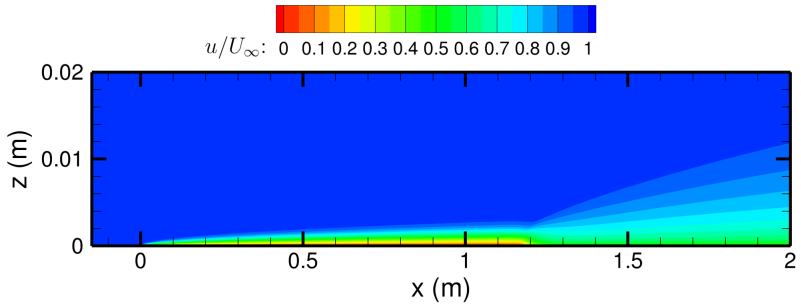

Fig. 5 Transitional flow over a flat plate computed with FUN3D at U_∞ = 34 m/s and $\mathrm{Re}_\infty = 2.26 \times 10^6$ m^{-1}. The location of transition onset is x_{tr} = 1.168 m.

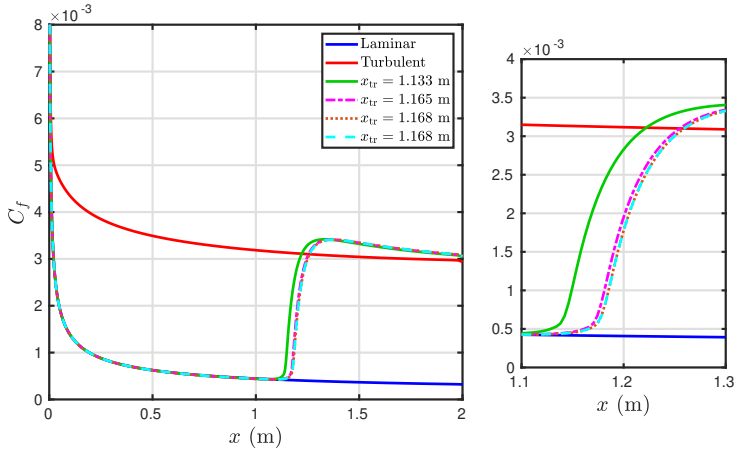

Fig. 6 Skin-friction distributions from laminar, transitional, and fully-turbulent basic states of flow over a flat plate computed with FUN3D at U_∞ = 34 m/s and $\mathrm{Re}_\infty = 2.26 \times 10^6$ m^{-1}. Here, the green solid line represents iteration one, the magenta dashed-dotted line corresponds to iteration two, the orange dotted line corresponds to iteration three, and the cyan dashed line represents the final iteration.

IV. NLF(1)-0416 Airfoil

Early work on transition to turbulence over subsonic airfoils has been done by Drela and Giles [23], along with Stock and Haase [24]. To help verify the automated iterative method in Figure 2, we consider subsonic flow over an NLF(1)-0416 airfoil. Two different cases are chosen for this geometry with a chord length of 1 m. The higher Reynolds number case ($\mathrm{Re}_c = 9 \times 10^6$) with $\alpha = 0°$ has no separation bubble, while the other case with $\mathrm{Re}_c = 4 \times 10^6$ and $\alpha = 5°$ has a separation bubble on the lower surface. We can verify our results with previous work, such as Zafar et al. [25] that predicted transition over an NLF(1)-0416 airfoil using machine learning, and with RANS-based transition models.

A. No Separation Bubble

For the case with no separation bubble, the freestream density, velocity, and temperature are $\rho_\infty = 4.78$ kg/m^3, $U_\infty = 34.7$ m/s, and $T_\infty = 300$ K, respectively. The freestream velocity is very similar to the flat-plate case and yields a freestream Mach number of $M_\infty = 0.1$. We consider an angle of attack equal to zero degrees. The left, right, top, and bottom edges of the computational domain are set to freestream boundary conditions. We employ adiabatic and no-slip boundary conditions at the airfoil surface. Figure 7 displays the streamwise-velocity contours for an initial transitional basic state at the selected flow parameters from FUN3D, which differs from the initial laminar FUN3D solution we used

for the 2D flat plate. The basic state in Figure 7 is computed with the SA turbulence model, where laminar regions have the turbulent production terms switched off. For the initial transitional basic state, we specified the location of transition onset at $x_{tr} = 0.4c$ for both the upper and lower surfaces of the NLF(1)-0416 airfoil. We show the pressure-coefficient and skin-friction distributions along the airfoil surfaces in Figure 8. From the skin-friction distribution, we can see transition occurs at $x_{tr} = 0.4c$ for both the upper and lower surfaces of the airfoil.

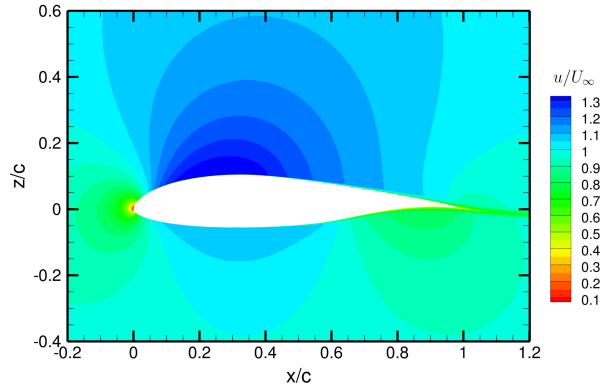

Fig. 7 Streamwise-velocity contours for the initial transitional FUN3D basic state of a NLF(1)-0416 airfoil at $\alpha = 0°$, $U_\infty = 34.7$ m/s, and $\mathrm{Re}_c = 9 \times 10^6$.

We employ an ultrafine C-grid from the AIAA Transition Modeling Workshop 1 to compute the NLF(1)-0416 basic state displayed in Figure 7 and the other FUN3D airfoil simulations. A total of 2113 and 289 grid points are used in the streamwise and wall-normal directions, respectively. The structured C-grids are converted into unstructured format while running with the FUN3D suite of codes, but that does not change the resolution or cell geometry. We compared the skin-friction and pressure-coefficient distributions on five coarser grids with the finest resolution grid showing no change from the second finest (not shown for brevity). The streamwise-velocity contours in Figure 7 look very smooth, and there is a well-defined stagnation point at the leading edge of the NLF(1)-0416 airfoil. Also, the streamwise distribution of pressure coefficient and the skin friction in Figure 8 look well resolved by the computational grid. The boundary layer is fully attached in this case, so the instabilities are purely of TS type.

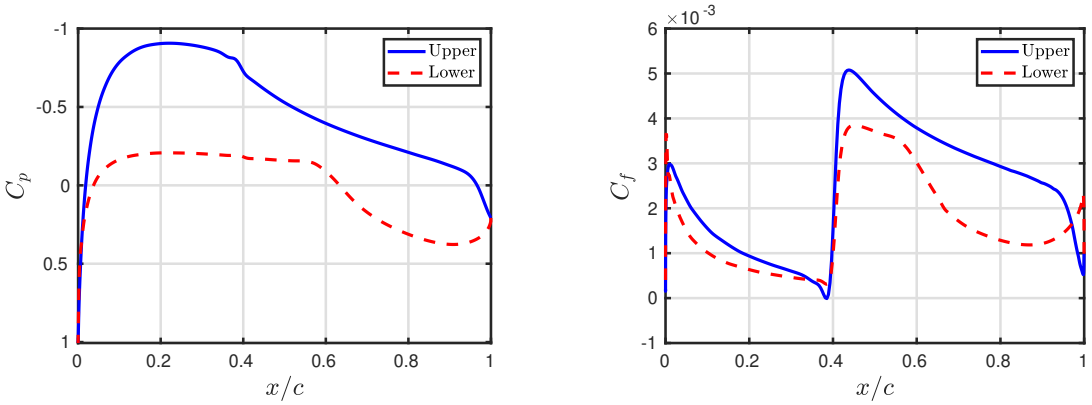

(a) Pressure coefficient on the airfoil surface.

(b) Skin friction on the airfoil surface.

Fig. 8 Distribution of the (a) pressure coefficient and (b) skin friction on the upper and lower surfaces of the NLF(1)-0416 airfoil at $\alpha = 0°$, $U_\infty = 34.7$ m/s, and $\mathrm{Re}_c = 9 \times 10^6$ with specified transition locations of $x_{tr,u} = 0.4c$ and $x_{tr,l} = 0.4c$.

After computing the initial FUN3D basic state for the NLF(1)-0416 airfoil, we calculate the N-factor envelopes with LASTRAC by using PSE and find the locations of transition onset for the upper and lower surfaces. Figure 9 displays the N-factor envelopes for the upper and lower airfoil surfaces from the basic state in Figure 7. The largest N-factor value is approximately 19.5 for the upper surface and 12 for the lower surface. Furthermore, the N-factor envelope for

the upper airfoil surface in Figure 9 looks similar to the N-factor envelopes in Figure 3(b) from Zafar et al. [25]. We obtain $N_{\text{tr}} = 7.2$ by substituting $Tu = 0.15\%$ into the equation $N_{\text{tr}} = -8.43 - 2.4\ln(Tu)$ from Mack [4]. Also, the value $N_{\text{tr}} = 7.2$ is given by the AIAA Transition Modeling Workshop 1. This results in a transition location of $x_{\text{tr}} = 0.3256c$ for the upper surface and $x_{\text{tr}} = 0.3172c$ for the lower surface of the NLF(1)-0416 airfoil. These values can now be enforced in the new FUN3D transitional basic state.

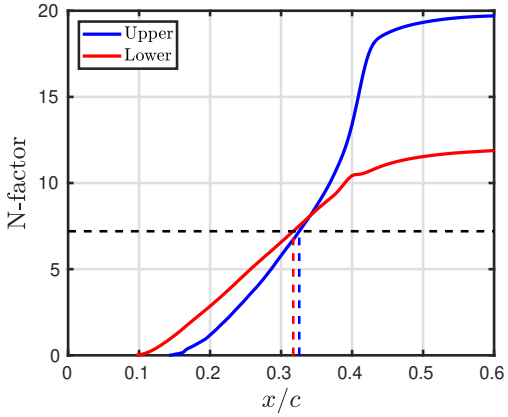

Fig. 9 N-factor envelope computed with LASTRAC about a transitional FUN3D basic state of flow over a NLF(1)-0416 airfoil at $\alpha = 0°$, $U_\infty = 34.7$ m/s, and $\text{Re}_c = 9 \times 10^6$.

We compute the N-factor envelopes for the NLF(1)-0416 airfoil surfaces by using PSE with LASTRAC about the new FUN3D basic state that has specified transition locations of $x_{\text{tr,u}} = 0.3256c$ and $x_{\text{tr,l}} = 0.3172c$. Figure 10 displays these N-factor envelopes with blue solid lines. From these envelopes, we calculate the new transition locations of $x_{\text{tr,u}} = 0.3171c$ and $x_{\text{tr,l}} = 0.3159c$ by finding out where $N_{\text{tr}} = 7.2$ intersects the N-factor curves. Afterward, we compute the next FUN3D transitional basic state with $x_{\text{tr,u}} = 0.3171c$ and $x_{\text{tr,l}} = 0.3159c$. The envelopes associated with this NLF(1)-0416 basic state are depicted in Figure 10 by red solid lines. This process is repeated three more times yielding final transition locations of $x_{\text{tr,u}} = 0.3089c$ and $x_{\text{tr,l}} = 0.3157c$ for the NLF(1)-0416 airfoil. All of the N-factor envelopes that correspond to different iteration numbers are shown in Figure 10. We can see the N-factor envelopes in Figure 10 eventually converge along with x_{tr} for the NLF(1)-0416 airfoil in a similar manner as the flat-plate case. Figure 11 displays the pressure-coefficient and skin-friction distributions on the upper and lower surfaces of the airfoil for many different FUN3D basic states. Notice both of these distributions converge with iteration number as well. Also, the flow transitions further upstream on the upper surface of the airfoil at $x_{\text{tr,u}} = 0.3089c$ than on the bottom surface at $x_{\text{tr,l}} = 0.3157c$, which is expected because of the adverse pressure gradient on the upper surface.

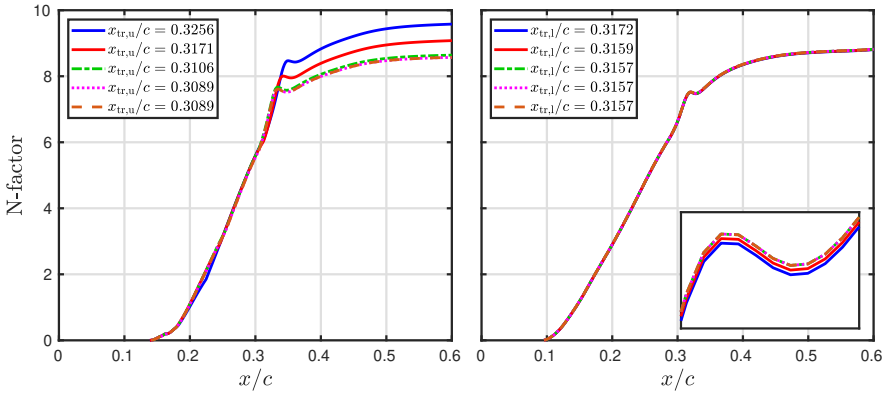

Fig. 10 N-factor envelopes computed with LASTRAC about several transitional FUN3D basic states of flow over a NLF(1)-0416 airfoil at $\alpha = 0°$, $U_\infty = 34.7$ m/s, and $\text{Re}_c = 9 \times 10^6$. The left plot is for the upper surface, and the right plot is for the lower surface.

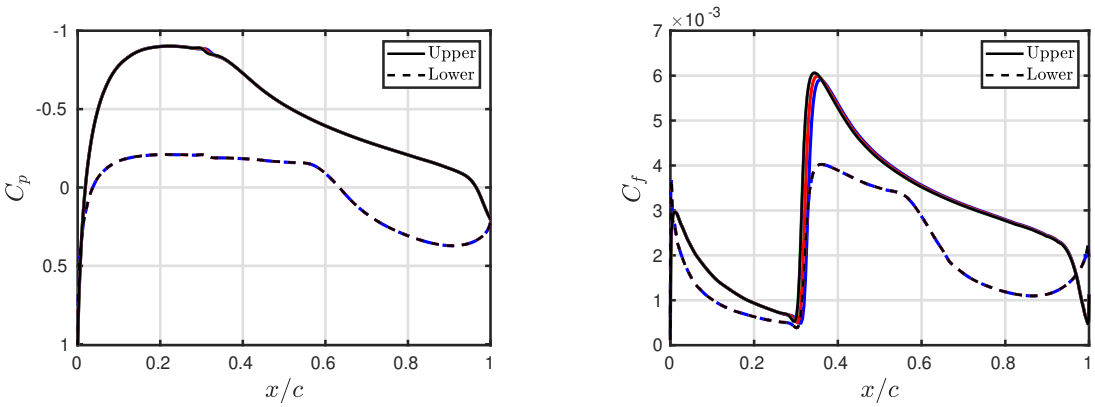

(a) Pressure coefficient on the airfoil surface. **(b) Skin friction on the airfoil surface.**

Fig. 11 Distributions of the (a) pressure and (b) skin-friction coefficients on the NLF(1)-0416 airfoil at $\alpha = 0°$, $U_\infty = 34.7$ m/s, and $\mathrm{Re}_c = 9 \times 10^6$. Here, iteration one is the blue line, iteration two is the red line, iteration three is the green line, iteration four is the magenta line, and the final iteration is the black line.

B. Separation Bubble on Lower Surface

For the case with a small separation bubble, the freestream density, velocity, and temperature are $\rho_\infty = 2.124$ kg/m^3, $U_\infty = 34.7$ m/s, and $T_\infty = 300$ K, respectively. We consider an angle of attack equal to five degrees. This case is significant because a typical LASTRAC workflow based on a single iteration of a FUN3D basic state and then stability analysis would not be enough to capture the strong influence of the separation bubble on transition. Note there is an interaction that occurs between the separation-reattachment characteristics and the location of transition onset. The boundary conditions are the exact same as the previous airfoil case with no separation bubble. Also, the computational grids are the exact same as the previous airfoil case. Figure 12 shows the N-factor envelopes computed about different FUN3D transitional basic states of an NLF(1)-0416 airfoil with $\mathrm{Re}_c = 4 \times 10^6$. We set $N_{\mathrm{tr}} = 7.2$ just as we did for the previous airfoil case. The locations of transition onset converge to $x_{\mathrm{tr,u}} = 0.2046c$ and $x_{\mathrm{tr,l}} = 0.6521c$ after four iterations. Figure 12 shows the iterative convergence of the N-factor envelopes. Hence, our iterative automated method still converges well even with the interaction that occurs between the separation-reattachment characteristics of the separation bubble and the location of transition to turbulence. For the lower airfoil surface, the location of transition also does not shift in one direction as it converges.

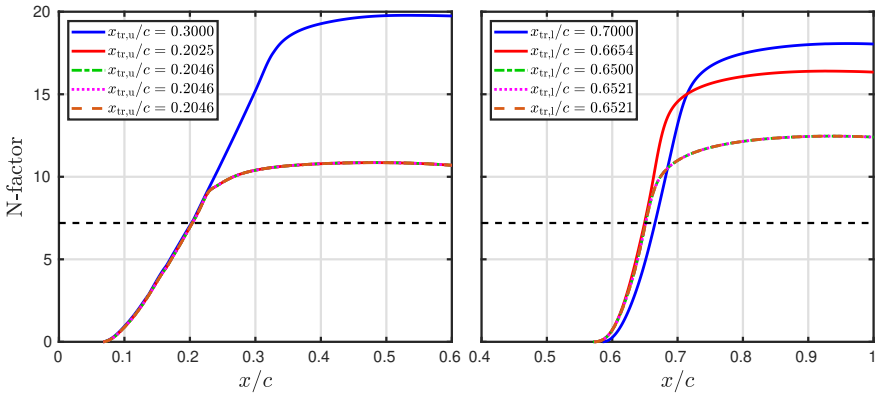

Fig. 12 N-factor envelopes computed with LASTRAC about several transitional FUN3D basic states of flow over a NLF(1)-0416 airfoil at $U_\infty = 34.7$ m/s, $\alpha = 5°$, and $\mathrm{Re}_c = 4 \times 10^6$. The left plot is for the upper surface, and the right plot is for the lower surface. Also, the black dashed line represents $N_{\mathrm{tr}} = 7.2$.

Figure 13 depicts the iterative convergence of both the pressure-coefficient and skin-friction distributions for the NLF(1)-0416 airfoil with an angle of attack equal to five degrees and $\mathrm{Re}_c = 4 \times 10^6$. There is a sizable shift between

the initial state and the first iteration, but after that both quantities converge quickly. The skin-friction distribution corresponding to iteration four shows the flow transitioning at $x_{\mathrm{tr,u}} = 0.2046c$ and $x_{\mathrm{tr,l}} = 0.6521c$ with a separation bubble on the lower airfoil surface. Transition at $x_{\mathrm{tr,u}} = 0.2046c$ and $x_{\mathrm{tr,l}} = 0.6521c$ is accompanied by a substantial rise in the skin friction. This rise is greater on the upper airfoil surface. Figure 14 compares the pressure-coefficient and skin-friction distributions for this case between the SST2003-LM2009 transition method [15] and the automated iterative method with the FUN3D and LASTRAC codes. Here, the SST2003-LM2009 transition method [15] is run with the FUN3D suite of codes. There is good agreement between the automated iterative method and the SST2003-LM2009 method in Figure 14. For both of these methods, the separation bubble on the lower surface of the airfoil is approximately the same size and occurs at roughly the same location. Results from this case with a separation bubble and the previous case without a separation bubble for subsonic flow over an NLF(1)-0416 airfoil demonstrate the accuracy and robustness of the iterative approach that is described in Figure 2. We are still in the process of examining how the initial transition location impacts the convergence process for the NLF(1)-0416 airfoil.

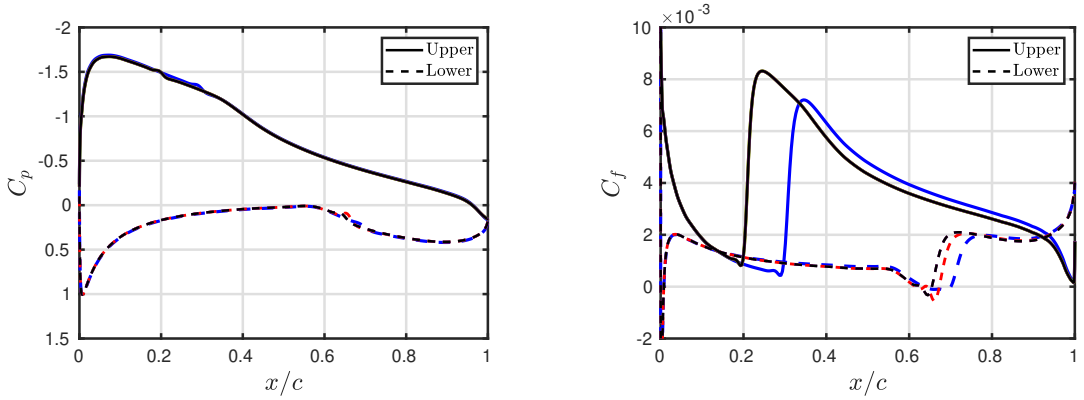

(a) Pressure coefficient on the airfoil surface. **(b) Skin friction on the airfoil surface.**

Fig. 13 Distributions of the (a) pressure and (b) skin-friction coefficients on the NLF(1)-0416 airfoil at $U_\infty = 34.7$ m/s, $\alpha = 5°$, and $\mathrm{Re}_c = 4 \times 10^6$. Here, the initial state is the blue line, iteration one is the red line, iteration two is the green line, iteration three is the magenta line, and the final iteration is the black line.

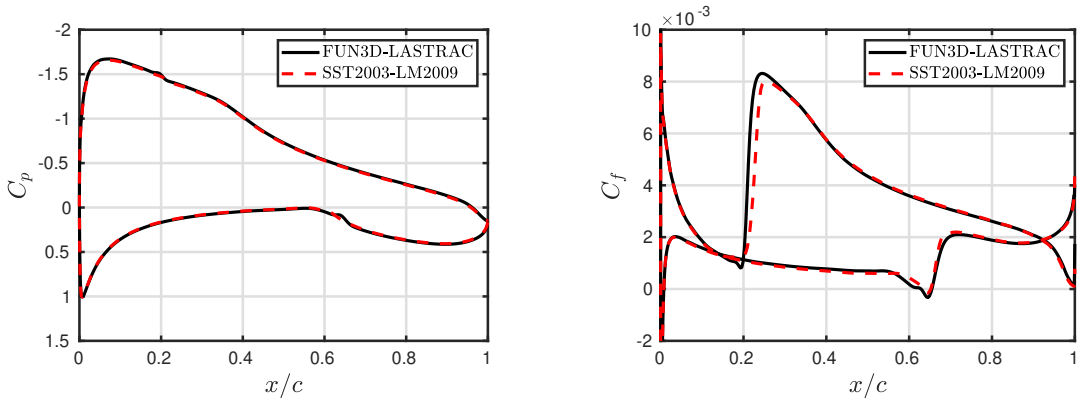

(a) Pressure coefficient on the airfoil surface. **(b) Skin friction on the airfoil surface.**

Fig. 14 Comparisons of the (a) pressure and (b) skin-friction coefficients on the NLF(1)-0416 airfoil at $U_\infty = 34.7$ m/s, $\alpha = 5°$, and $\mathrm{Re}_c = 4 \times 10^6$ between the SST2003-LM2009 method [15] and the automated iterative method.

V. 6:1 Prolate Spheroid

We consider low-speed flow over a 6:1 prolate spheroid that can transition via TS waves and/or CF instability to extend and evaluate the automated iterative transition prediction method. Results in this section are preliminary and will

focus on CF effects. This particular flow configuration is a part of both the AIAA Transition Modeling Workshop and the AVT-313 Incompressible Flow Transition Comparison Workshop (`http://web.tecnico.ulisboa.pt/ist12278/Workshop_AVT_313_2D_cases/Workshop_AVT_313_2D_cases.htm`). Past work on the prolate spheroid includes experimental work by Kreplin et al. [26] and computational work by Krimmelbein et al. [27]. Spall and Malik [28] also examined the stability of three-dimensional boundary layers over a 6:1 prolate spheroid. The freestream Mach number, temperature, and Reynolds number based on the spheroid length are 0.13, 300 K, and 6.5×10^6, respectively. We consider angles of attack equal to 10 and 15 degrees. We set the left, right, top, and bottom edges of the computational domain to freestream boundary conditions. Adiabatic and no-slip boundary conditions are enforced on the entire surface of the 6:1 prolate spheroid.

Figure 15 shows the skin-friction contours for the initial FUN3D basic state of a 6:1 prolate spheroid with $x_{tr}/L = 0.6$. We use a multiblock structured grid that is nonsingular and has three blocks. Two of the blocks are located near the stagnation points, and each one has a resolution of $65 \times 65 \times 257$ grid points. The middle block has a resolution of $321 \times 193 \times 257$ grid points. We convert this multiblock structured grid to unstructured format with 17,825,792 hexahedrals so that we can run it with the FUN3D suite of codes. Results are compared to lower resolution grids with 7,520,256 and 2,228,224 hexahedrals with small changes in the skin-friction contours and transition locations (not shown). Figure 16 depicts the inviscid streamlines generated by 65 vertex seeds in our solver-independent module [21] on the spheroid. For the convenience of analyzing and presenting the results, we place the streamline seeds regularly along the azimuth at $x/L = 0.5$. However, we could have also used a random array of seed locations generated in an automated manner by the solver-independent module [21]. The same 65 streamlines are used for every angle of attack to compute the N-factor distribution with LASTRAC. We compared the LASTRAC stability results with 65 and 150 streamlines (not shown), which indicated that 65 regularly-spaced streamlines is sufficient to resolve the transition front at every angle of attack that is considered in this paper.

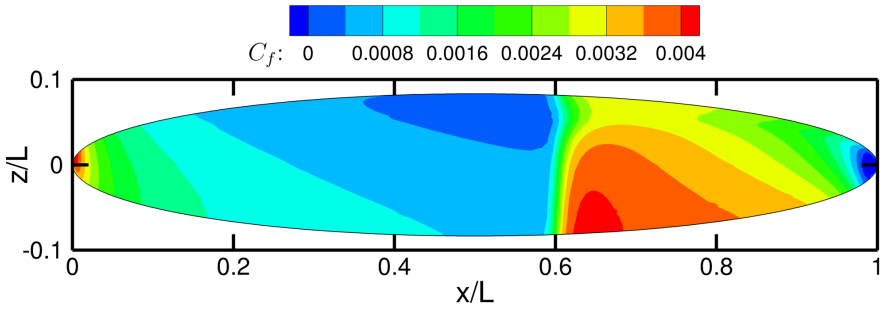

Fig. 15 Skin-friction contours for the initial transitional FUN3D basic state of a 6:1 prolate spheroid with $Re_L = 6.5 \times 10^6$. The onset of transition is set to $x_{tr}/L = 0.6$.

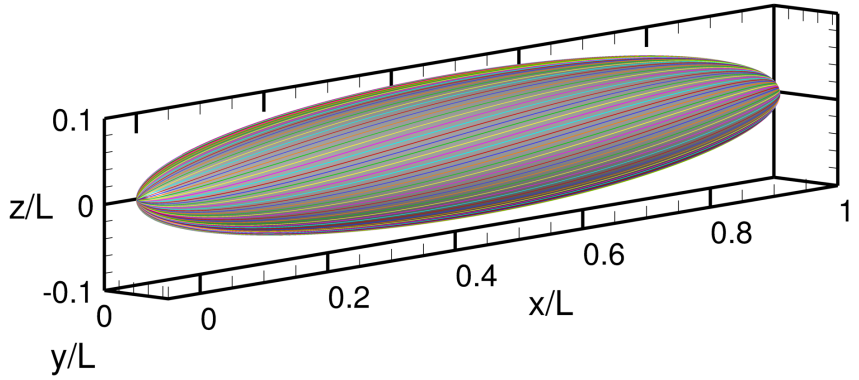

Fig. 16 Streamlines generated by 65 vertex seeds used for PSE with LASTRAC.

After computing the FUN3D basic state and generating 65 inviscid streamlines, the transition analysis module used the LST and PSE functionality within LASTRAC to calculate the surface N-factor distributions from stationary CF

instability. Figure 17 displays the N-factor contours that correspond to stationary CF instability for the 6:1 prolate spheroid at $\alpha = 10°$ from LST and PSE. Notice the solutions from LST and PSE indicate transition occurs due to stationary CF instability over a majority of the spheroid surface. LST results in a solution where transition happens slightly more upstream than in the PSE solution. Figure 17 has fairly similar N-factor contours to the ones in Figure 8 of Chang [21]. We are still in the process of utilizing the dual $N_{TS} - N_{CF}$ criterion [29–31] to determine where transition occurs. Once this process is finished, we plan to enforce the computed transition front on the spheroid surface and repeat the procedure in Figure 2 until convergence.

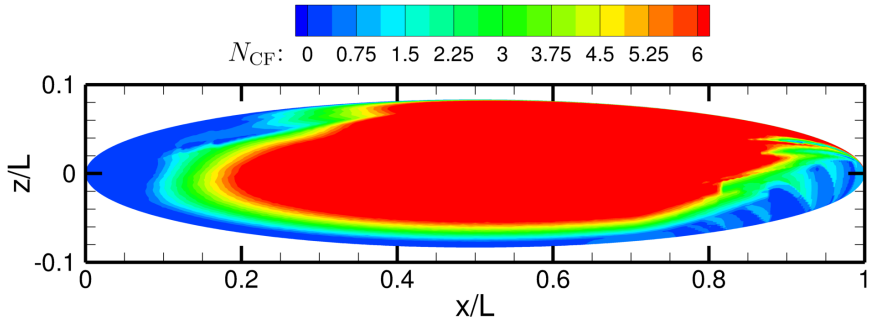

(a) CF N-factor contours from LST.

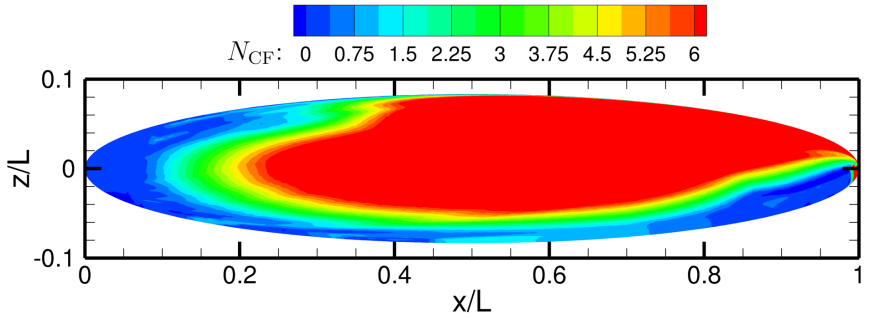

(b) CF N-factor contours from PSE.

Fig. 17 N-factor contours based on stationary CF instability from (a) LST and (b) PSE for a 6:1 prolate spheroid with $\alpha = 10°$ and $Re_L = 6.5 \times 10^6$ from LASTRAC.

For an angle of attack equal to fifteen degrees, we compute a similar FUN3D transitional basic state as in Figure 15 with a location of transition onset set to $x_{tr}/L = 0.8$. We employ the same grid and 65 streamlines as the previous cases. Figure 18 displays the N-factor contours that correspond to CF instability for the 6:1 prolate spheroid at $\alpha = 15°$. We see in Figure 18 that stationary CF instability appears to be significant over a large region of the spheroid body at this angle of attack. Based on CF N-factors alone, transition occurs slightly more upstream on the spheroid surface for this angle of attack compared to the previous case with $\alpha = 10°$. We plan to compare our spheroid results to past experimental [26] and computational [27] work once we fine tune the process of calculating the 3D transition front.

VI. Conclusion

Transition models that rely on RANS-based transport equations can be easily integrated into existing CFD codes. However, a weaker link to the underlying transition physics limits the accuracy of these models to the range of empirical correlations used during the model development. Transition prediction based on linear stability theory has the advantage of a stronger coupling with physics, however, the stability computations are difficult to automate and/or to integrate into large-scale CFD computations. They also require higher boundary-layer resolution and significant user expertise. To help address the need for a fully-integrated transition prediction method within routine CFD computations, we have presented an iterative approach that combines linear stability analysis with an unstructured CFD code that requires minimal user input. This approach couples the FUN3D unstructured flow solver with the LASTRAC stability code in order to simulate various transitional flow configurations. FUN3D is widely used for aerospace applications, but is

known for having a rather limited transition modeling capability based on the Langtry-Menter RANS model, which has been shown to fail by multiple contributors of the AIAA and AVT-313 and transition workshops for the prolate spheroid. Also, the coupling with LASTRAC allows transition N-factors based on the more prevalent quasiparallel stability analysis or the higher-fidelity PSE analysis that incorporates the effects of surface curvature and a nonparallel mean flow. A lot of work remains to be done in order to provide a comprehensive validation of this automated iterative capability, but the current paper is a good foundation for these extensions.

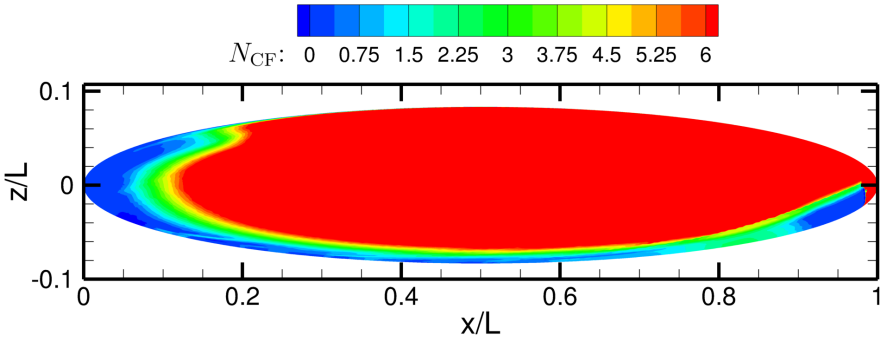

Fig. 18 N-factor contours based on stationary CF instability for a 6:1 prolate spheroid with $\alpha = 15^\circ$ and $Re_L = 6.5 \times 10^6$ from LASTRAC.

First, we considered low-speed flow over a 2D flat plate. The basic states were computed with FUN3D and had laminar, transitional, and fully-turbulent regions. We enforced the location of transition onset from the LASTRAC stability calculations (i.e., where N_{tr} intersects the N-factor envelope) in the FUN3D basic states. The resulting transitional FUN3D basic state for the flat plate agreed with our previous computations based on PSE/HLNSE [22] and the experiments performed by Wang and Gaster [20]. The automated iterative method reached iterative convergence in four iterations for a flat-plate case. We also considered flow over an NLF(1)-0416 airfoil at two different Reynolds numbers and angles of attack. The case with a smaller Reynolds number and larger angle of attack produced a small separation bubble on the lower airfoil surface. We saw the N-factor envelopes from the LASTRAC stability calculations were similar to the ones computed in Zafar et al. [25] at the same flow conditions. Also, the case with a smaller Reynolds number and larger angle of attack resulted in good agreement with the SST2003-LM2009 transition method [15]. Each of the NLF(1)-0416 cases reached convergence after five iterations. Lastly, we presented preliminary results for the 6:1 prolate spheroid, where low-speed flow can transition via TS waves and/or CF instability (focused on CF effects). We plan to compute the 3D transition front with the dual $N_{TS} - N_{CF}$ criterion and compare to experimental [26] and computational [27] work in the future. A similar analysis is being carried out with the structured OVERFLOW code to better demonstrate the solver-independent functioning of the iterative transition analysis. These results will be included in a forthcoming conference paper.

Acknowledgments

The computations described in this paper were carried out in support of the Revolutionary Computational Aerosciences discipline under the Transformational Tools and Technologies project of the NASA Transformative Aeronautics Concepts Program.

References

[1] Slotnick, J., Khodahoust, A., Alonso, J., Darmofal, D., Gropp, W., and Mavriplis, D., "CFD Vision 2030 Study: A Path to Revolutionary Computational Aerosciences," NASA/CR-2014-218178, 2014.

[2] Smith, A., and Gamberoni, A., "Transition, pressure gradient, and stability theory," Douglas Aircraft Co., Report No. ES26388, 1956.

[3] Ingen, J. V., "A suggested semi-empirical method for the calculation of the boundary layer transition region," Univ. of Technology, Report No. UTH1-74, 1956.

[4] Mack, L., "Transition prediction and linear stability theory," *Laminar-Turbulent Transition*, CP-224, AGARD, 1977, pp. 1–22.

[5] Crouch, J. D., and Ng, L., "Variable N-Factor Method for Transition Prediction in Three-Dimensional Boundary Layers," *AIAA Journal*, Vol. 38, No. 2, 2000, pp. 211–216. doi:https://arc.aiaa.org/doi/10.2514/2.973.

[6] Herbert, T., "Parabolized stability equations," *Annual Review of Fluid Mechanics*, Vol. 29, 1997, pp. 245–283. doi: https://doi.org/10.1146/annurev.fluid.29.1.245.

[7] Menter, F. R., Langtry, R. B., and Volker, S., "Transition Modelling for General Purpose CFD Codes," J. Flow, Turbulence and Combustion," *Journal of Flow, Turbulence, and Combustion*, Vol. 77, 2006, pp. 277–303.

[8] Perraud, J., Arnal, D., Casalis, G., Archambaud, J.-P., and Donelli, R., "Automatic Transition Predictions Using Simplified Methods," *AIAA Journal*, Vol. 47, No. 11, 2009, pp. 2676–2684.

[9] Coder, J. G., and Maughmer, M. D., "Computational Fluid Dynamics Compatible Transition Modeling Using an Amplification Factor Transport Equation," *AIAA Journal*, Vol. 52, No. 11, 2014, pp. 2506–2512.

[10] Krumbein, A., Krimmelbein, N., and Grabe, C., "Streamline-Based Transition Prediction Techniques in an Unstructured Computational Fluid Dynamics Code," *AIAA Journal*, Vol. 55, No. 5, 2017, pp. 1548–1564.

[11] Halila, G. L. O., Chen, G., Shi, Y., Fidkowski, K. J., and Martins, J. R. R. A., "High-Reynolds Number Transitional Flow Prediction using a Coupled Discontinuous-Galerkin RANS PSE Framework," AIAA Paper 2019-0974, 2019.

[12] Halila, G. L. O., Fidkowski, K. J., and Martins, J. R. R. A., "Toward Automatic Parabolized Stability Equation-Based Transition-to-Turbulence Prediction for Aerodynamic Flows," *AIAA Journal*, Vol. 59, No. 2, 2020, pp. 462–473.

[13] Anderson, W. K., and Bonhaus, D. L., "Implicit upwind algorithm for computing turbulent flows on unstructured grids," *Computer and Fluids*, Vol. 23, No. 1, 1994, pp. 1–22.

[14] Chang, C.-L., "Langley Stability and Transition Analysis Code (LASTRAC) Version 1.2 User Manual," NASA TM-2004-213233, URL: https://ntrs.nasa.gov/search.jsp?R=20040082550, 2004.

[15] Langtry, R. B., and Menter, F. R., "Correlation-based transition modeling for unstructured parallelized computational fluid dynamics codes," *AIAA Journal*, Vol. 47, No. 12, 2009, pp. 2894–2906.

[16] Spalart, P. R., and Allmaras, S. R., "A One-Equation Turbulence Model for Aerodynamic Flows," *Recherche Aerospatiale*, , No. 1, 1994, pp. 5–21.

[17] Lee-Rausch, E. M., Frink, N. T., Mavriplis, D. J., Rausch, R. D., and Milholen, W. E., "Transonic Drag Prediction on a DLR-F6 Transport Configuration Using Unstructured Grid Solvers," AIAA Paper 2004-556, 2004.

[18] Biedron, R. T., Carlson, J.-R., Derlaga, J. M., Gnoffo, P. A., Hammond, D. P., Jones, W. T., Kleb, B., Lee-Rausch, E. M., Nielsen, E. J., Park, M. A., Rumsey, C. L., Thomas, J. L., Thompson, K. B., and Wood, W. A., "FUN3D manual: 13.6," NASA TM 2019-220416, 2019.

[19] Chang, C.-L., "LASTRAC.3d: Transition Prediction in 3D Boundary Layers," AIAA Paper 2004-2542, 2004.

[20] Wang, Y., and Gaster, M., "Effect of surface steps on boundary layer transition," *Experiments in Fluids*, Vol. 39, No. 4, 2005, pp. 679–686. doi:https://doi.org/10.1007/s00348-005-1011-7.

[21] Chang, C.-L., "Development of Physics-Based Transition Models for Unstructured-Mesh CFD Codes Using Deep Learning Models," AIAA Paper 2021-2828, 2021.

[22] Hildebrand, N., Choudhari, M. M., and Paredes, P., "Predicting boundary-layer transition over backward-facing steps via linear stability analysis," *AIAA Journal*, Vol. 58, No. 9, 2020, pp. 3728–3734. doi:https://arc.aiaa.org/doi/10.2514/1.J059713.

[23] Drela, M., and Giles, M. B., "Viscous-Inviscid Analysis of Transonic and Low Reynolds Number Airfoils," *AIAA Journal*, Vol. 25, No. 10, 1987, pp. 1347–1355.

[24] Stock, H. W., and Haase, W., "Navier-Stokes Airfoil Computations with eN Transition Prediction Including Transitional Flow Regions," *AIAA Journal*, Vol. 38, No. 11, 2000, pp. 2059–2066.

[25] Zafar, M. I., Xiao, H., Choudhari, M. M., Li, F., Chang, C.-L., Paredes, P., and Venkatachari, B., "Convolutional neural network for transition modeling based on linear stability theory," *Physical Review Fluids*, Vol. 5, 2020, p. 113903.

[26] Kreplin, H.-P., Vollmers, H., and Meier, H. U., "Wall shear stress measurements on an inclined prolate spheroid in the DFVLR 3M × 3M low speed wind tunnel, Göttingen," Data Report IB 222-84 A 33, DFVLR – Deutsche Forschungs- und Versuchsanstalt für Luft- und Raumfahrt, DFVLR-AVA, 1985.

[27] Krimmelbein, N., Krumbein, A., and Grabe, C., "Validation of Transition Modeling Techniques for a Simplified Fuselage Configuration," AIAA Paper 2018-0030, 2018.

[28] Spall, R. E., and Malik, M. R., "Linear Stability of Three-Dimensional Boundary Layers over Axisymmetric Bodies at Incidence," *AIAA Journal*, Vol. 30, No. 4, 1992, pp. 905–913.

[29] Horstmann, K., Redeker, G., Quast, A., Dressler, U., and Bieler, H., "Flight Test with a Natural Laminar Flow Glove on a Transport Aircraft," AIAA Paper 1990-3044, 1990.

[30] Arnal, D., "Boundary Layer Transition: Prediction Based on Linear Theory," Special course on Progress in Transition Modeling, AGARD. R-793, 1994.

[31] Paredes, P., Venkatachari, B., Choudhari, M. M., Li, F., Hildebrand, N., and Chang, C.-L., "Transition Analysis for the CRM-NLF Wind Tunnel Configuration," AIAA Paper 2021-1431, 2021.

[32] Langtry, R. B., Sengupta, K., Yeh, D. T., and Dorgan, A. J., "Extending the $\gamma - Re_\theta$ correlation based transition model for crossflow effects," AIAA Paper No. 2015-2474, 2015.